

Distant Damage-Assessment Method for Multilayer Composite Systems Using Electromagnetic Waves

Tzu-Yang Yu, A.M.ASCE¹

Abstract: In this paper, a damage assessment method for remotely inspecting the near-surface condition of multilayer composite systems is proposed. The method utilizes far-field steady-state electromagnetic waves reflected from the surface of multilayer composite systems and generates the in-depth profile of the inspected composite systems using inverse synthetic aperture radar (ISAR) imaging technique. Spatial imagery of the system can be reconstructed with the structural and geometric features of the multilayer system. These features are revealed by discrete scatterers in the imagery. Reconstructed imagery can be used for detecting construction defects and structural damages in the near-surface region of the system. The theoretical background of the method is described, followed by experimental measurements on glass-fiber-reinforced polymer (GFRP)-confined concrete cylinders with an artificial defect as an example of multilayer composite systems. Continuous waves in the frequency range of 8 to 12 GHz were used. The imaging results show that the proposed method can reveal the location and size of the embedded defect in the GFRP-concrete composite system, indicating the potential use of the method as a basis for distant radar/microwave nondestructive testing/evaluation techniques in civil engineering. DOI: 10.1061/(ASCE)EM.1943-7889.0000257. © 2011 American Society of Civil Engineers.

CE Database subject headings: Damage; Assessment; Concrete; Radar; Microwaves; Fiber reinforced polymer; Inspection; Composite structures.

Author keywords: Damage assessment; Concrete; Radar; Fiber-reinforced polymers; Tomographic reconstruction.

Introduction

Damage assessment of multilayer composite systems has been an important topic in civil engineering for improving the safety of (1) existing systems strengthened with externally wrapped composites, and (2) laminated/sandwich composite systems. Existing structures are strengthened, repaired, and rehabilitated with externally wrapped/bonded high-performance composites for the demonstrated effectiveness and efficiency of externally strengthening techniques. Such techniques have been reported on reinforced concrete (RC) and prestressed concrete (PC) structures (Saadatmanesh et al. 1991; Meier 1995; Rahami and Hutchinson 2001; Correia et al. 2009; Janke et al. 2009), steel structures (Zhao and Zhang 2007), masonry structures (Lissel et al. 2003; Shrive 2006; Grande et al. 2008), timber structures (Radford et al. 2002; Dobrila and Premrov 2003), and offshore structures (McGeorge et al. 2009). Moreover, laminated/sandwich composite systems are found in structural elements made of composite materials, such as bridge decks (Kumar et al. 2004; Keller and Schollmayer 2004), pipelines (Chen and Leib 1993; Lam et al. 2003), and wind turbines (Bechly and Clausen 1997; Kensch 2006; Marin et al. 2008; Hameed et al. 2009). With the need from rapid strengthening and high-performance composites made available for civil engineers, multilayer composite systems are frequently encountered in the routine maintenance of civil infrastructure.

In these systems, construction defects (e.g., air voids) and stress-induced delamination (e.g., debonding, decohesion) can lead to the reduction in bearing capacity and result in immature brittle failures of the multilayer composite systems. One example is the failure of fiber-reinforced polymer (FRP)-strengthened concrete structures. FRP-strengthened concrete structures are less ductile than traditional RC structures because of the limited deformability provided by FRP composites. This suggests a reduction of the plastic deformability in FRP-concrete composite systems and a brittle or semibrittle failure mode that should be avoided in the ultimate state of the structures. Structural damages, such as concrete cracking or crumbling inside the FRP wrapping, and/or debonding of the FRP sheet from concrete, may occur under various degrees of confinement pressure provided by the FRP wrap. These types of failures have been observed in FRP-confined concrete specimens (Au and Buyukozturk 2005), and also FRP-confined large-scale RC structures (Sheikh and Yau 2002). Additionally, construction defects, such as trapped air voids or pockets (material separation), can occur at the interface between FRP sheets/plates and the substrate concrete during the cast-in-place construction. Under mechanical loads, stress concentrations can develop around these air voids, leading to further development of FRP debonding from the concrete substrate in the near-surface region. Another example is the fatigue failure of wind turbines caused by the presence of air voids (Chambers et al. 2006) and composite delamination (Kensch 2006; Marin et al. 2008). The theoretical background of composite delamination has also been investigated by Chen and Leib (1993).

Both structural damages and construction defects can lead to brittle, premature failures of multilayer composite systems, which need to be detected and repaired for the safety, sustainability, and efficient maintenance of the systems. To achieve the goal, damage assessment techniques are needed for detecting damage and defects, such as air voids and delaminations, in multilayer composite

¹Assistant Professor, Dept. of Civil and Environmental Engineering, Univ. of Massachusetts–Lowell, Lowell, MA 01854. E-mail: tzyang_yu@uml.edu

Note. This manuscript was submitted on January 19, 2010; approved on February 23, 2011; published online on February 25, 2011. Discussion period open until January 1, 2012; separate discussions must be submitted for individual papers. This paper is part of the *Journal of Engineering Mechanics*, Vol. 137, No. 8, August 1, 2011. ©ASCE, ISSN 0733-9399/2011/8-547-560/\$25.00.

systems. In this paper, a distant damage assessment method is proposed for the inspection of multilayer composite systems in civil engineering. Distant inspection represents several advantages over contact/near-contact inspection for large-scale civil infrastructure, such as the inspection ease on structures in remote areas. The proposed distant damage assessment method mainly consists of an image reconstruction component for projecting complex distant measurements onto a spatial domain as reconstructed images and a morphological processing component for quantifying the information contained in the images. Glass-fiber-reinforced polymer (GFRP)-confined concrete cylinders with artificial near-surface defects were used as an example multilayer composite system in the development of the method. Laboratory far-field complex electromagnetic (EM) measurements (reflection response) of the cylinders were collected.

In what follows, several inspection methods using EM measurements on GFRP-concrete structures are reviewed. Theoretical background of the proposed method is provided, followed by the application of the method on GFRP-confined concrete cylinders. Imaging and assessment results are provided with discussions. Finally, research findings and issues are summarized in the conclusion.

Review of Damage Assessment Methods Using EM Waves

Damage assessment using EM waves is usually conducted by microwave or radar nondestructive testing (NDT) techniques characterized by the frequency spectrum in which the chosen EM waves belong. Although the microwave spectrum (300 MHz to 30 GHz) is included in the radio frequency (RF) spectrum (300 Hz to 110 GHz), the term “microwave NDT” has also been used interchangeably with “radar NDT” in civil engineering. EM waves can be produced and collected by different devices such as antenna, waveguide, and coaxial probe. Most used EM waves are in the frequency range from very high frequency (VHF) (30 MHz to 300 MHz) to super high frequency (SHF) (3 GHz to 30 GHz) for the applications including material characterization (Al-Qadi et al. 1995; Bois et al. 2000; Arunachlam et al. 2006), bridge pier scour detection (Millard et al. 1998; Forde et al. 1999), void and crack detection in stone and masonry structures (Binda et al. 1998; Maierhofer et al. 2001), damage detection in sluices (Maierhofer et al. 1998), fatigue cracks detection in steel structures (Qaddoumi et al. 2000), concrete cover thickness detection (Klysz et al. 2004), concrete cracking detection (Buyukozturk and Rhim 1995; Rhim and Buyukozturk 2000; Maierhofer et al. 2003; Nadakuduti et al. 2006), rebar detection (Rhim and Buyukozturk 2000; Shaw et al. 2005), and structural testing and remote sensing (Farrar et al. 1999; Shinozuka et al. 2000; Pieraccini et al. 2004). Frequencies used for detecting underground and underwater objects are usually less than 1 GHz to achieve better penetration. For detecting anomalies (air voids, rebar) in concrete, higher frequencies (greater than 1 GHz) are usually adopted for better resolution. Frequencies chosen for material characterization are widely distributed because of different experimental configurations. Additional general information on the use of microwave/radar NDT in civil engineering can be found in the literature (Blitz 1997; Yu 2009).

For the damage assessment problem of FRP-concrete systems in which the near-surface debonding is targeted for detection, both near-field and far-field EM measurements have been used. Li and Liu (2001) applied a bistatic radar NDT system to detect air voids in the interface region between GFRP-epoxy layer/jacket

and concrete surfaces. Radar measurements were collected at a frequency of 10 GHz by using a pair of dielectric lenses for signal focusing. The imagery of the structure was the assembly of reflection coefficients at various spatial points. The presence of damages and defects was represented by the variation of reflection coefficients. Feng et al. (2002) used a horn antenna and a waveguide reflectometer for detecting air voids in the interface region of GFRP-confined concrete specimens. Dielectric lenses were introduced to mechanically focus plane waves on a localized spot inside the specimens to enhance the strength of reflected signals. Reflection coefficients were used for evaluating the difference between intact and damaged responses. Later, Kim et al. (2004) proposed the use of planar slot antenna arrays for detecting air voids in concrete panel and block specimens. The in-depth imagery was the assembly of the coefficients associated with the Hankel function used to decompose reflection coefficient. The focusing intensity in the imagery was used to indicate the presence and location of damages. Akuthota et al. (2004) used an open-ended rectangular waveguide probe and near-field radar measurements for detecting disbands and delaminations between carbon-FRP (CFRP) laminate and the concrete substrate. Transmitted EM waves were linearly polarized with orientation orthogonal to the unidirectional carbon fibers to achieve strong penetration through the CFRP laminate. Beyond the use of microwave/radar NDT, a comprehensive review of other NDT methods for the damage assessment of FRP-concrete systems, including acoustic/ultrasound methods, passive and active infrared (IR) thermography (Kurita et al. 2009), can be found in Yu (2009).

From the review on the damage assessment methods for FRP-concrete structures using EM waves, it is found that (1) reflected EM waves are reportedly feasible for revealing the in-depth condition of the structures; (2) near-field measurements (inspection distance usually less than 1 m) are typically required to perform in-depth assessment of the structures; (3) spatial images are generally needed for locating defects; (4) improvement of image resolution in near-field methods is usually performed by mechanical devices, requiring specially designed antenna arrays or lens with various shapes and dimensions; (5) far-field measurements are generally used for reconstructing surface profiles of structures; and (6) damage assessment by using either one-dimensional signals or two-dimensional images is manually and qualitatively performed in many techniques, suggesting the need for subjective evaluation.

On the basis of these findings, a distant inspection technique using reflected far-field EM waves is proposed. In-depth assessment is conducted by processing the complex EM measurements (amplitude and phase) into spatial images by using back-projection algorithms. In the proposed method, image resolution is numerically improved by including additional measurements at different frequencies and incident angles of inspection. Reconstructed images are quantitatively and automatically evaluated by the use of mathematical morphology. In what follows, theoretical background of the method is introduced, and an application of the method on GFRP-concrete cylinders is provided.

Theory and Application of the Method

The proposed damage assessment method consists of two major steps; an image reconstruction process and an image interpretation process. The image reconstruction processing transforms measured distant (far-field), reflected EM waves from a target structure to spatial images depicting the in-depth profile (range-cross range) of the structure by using back-projection algorithms. The image interpretation processing characterizes the back-projection images

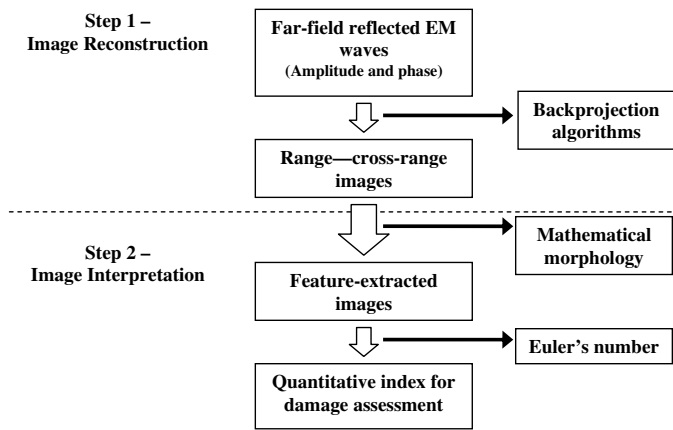


Fig. 1. Overview of the proposed damage assessment methodology

by quantifying the images using mathematical morphology. Fig. 1 shows the overview of the proposed method.

In the reconstructed in-depth profile (range-cross-range images or back-projection images) of a structure, the presence of near-surface defects is represented by scattering signals in the images. This transformation is achieved by the integrated use of inverse synthetic aperture radar (ISAR) measurements and back-projection algorithms. The transformation projects physical signals (EM waves) onto a spatial plane where the magnitude of image pixels indicates the intensity of EM wave scattering. The image interpretation processing utilizes techniques in mathematical (or quantitative) morphology such as erosion and dilation to extract the features of reconstructed back-projection images. Quantification of images is performed on the feature-extracted images, using Euler's number as a measure.

Theory

Image Reconstruction Processing

Far-Field Reflected EM Waves

In the measurements of reflected EM waves, the target structure is inspected by one radar antenna used as the signal transmitter and the receiver (monostatic mode). Far-field ISAR measurements are collected by measuring the reflection response of the target structure along a synthetic aperture that is defined by the range of azimuth angle or total inspection angle, θ_{int} . The far-field condition is satisfied by deploying the radar at a distance beyond the far-field distance d_{ff} generally defined by (Skolnik 1990)

$$d_{ff} = \frac{2D^2}{\lambda} \quad (1)$$

where D = largest dimension of antenna apertures; and λ = minimum wavelength. Transmitted radar signals (EM waves) are approximately plane waves beyond the far-field distance, whose accuracy can be evaluated by a wave-front error $E_r^{wf}(r)$ and a phase error $E_r^{ph}(r)$ (Yu and Buyukozturk 2008)

$$E_r^{wf}(r) = \frac{D^2}{8r} \quad (2)$$

$$E_r^{ph}(r) = \frac{\pi D^2}{4r} \quad (3)$$

where r = range distance or the inspection range. Cross range is defined as the direction perpendicular to the range direction. ISAR measurements are the SAR measurements collected by the radar orbiting the target structure at a constant range distance.

Fig. 2 illustrates the physical inspection scheme in which far-field ISAR measurements are collected. In Fig. 2, the radar begins transmitting continuous waves to the target structure at one frequency, collecting steady-state reflection responses, and shifting to next frequency on a starting position. It moves to the next position on the synthetic aperture and repeats the same procedure.

After completing the measurements over the entire angular (from 0 to θ_{int}) and frequency (from ω_{min} to ω_{max}) range, the frequency-angle measurements (amplitude and phase) are obtained, and a data plane (ω, θ) is consequently constructed, as shown in Fig. 3. On this data plane, integration of various amounts of far-field ISAR measurements is equivalent to reconstructing images by using different areas on the data plane. In addition, image resolutions are gradually improved with the increase of the area on the data plane.

In-depth profiles or range-cross-range images of the target structure are generated by tomographic reconstruction methods (Kak and Slaney 1999) by using the far-field ISAR measurements. The used tomographic reconstruction method is implemented by a time-domain back-projection algorithm for the efficiency and flexibility offered by the algorithm. Each pixel in the back-projection images is reconstructed by coherently integrating the far-field ISAR measurements over the ranges of incident frequency and azimuth angle. Processing efficiency is provided by dividing the entire aperture into several subapertures and performing one-dimensional (1D) inverse Fourier transformation (IFT) for each subaperture (Yegulap 1999). Coherent integration/summation is conducted by time-shifting and space-aligning the signal collected at each aperture position for every pixel in the image. This integration can be performed with subaperture and subband measurements. Complete

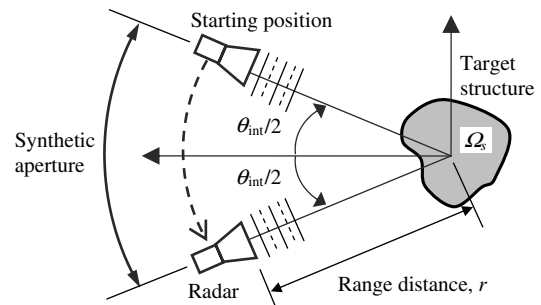


Fig. 2. Far-field ISAR measurements

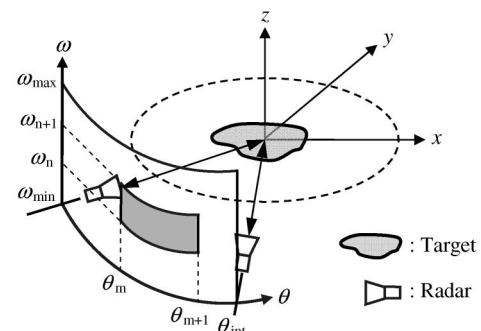


Fig. 3. Physical coordinates and the data plane (ω, θ)

reconstruction is accomplished after the integration is done throughout the entire data plane. Processing flexibility is offered by the option of rendering images at subaperture level, rather than after collecting and storing all the measurements along the aperture.

Collected far-field ISAR measurements are processed by back-projection algorithms whose principles are provided in the following section.

Principles of Back-Projection Algorithms

Consider the planar scattering problem in a domain Ω_s containing N point scatterers (Fig. 4) and an incident wave with unit amplitude to be (Kong 2000)

$$\psi_{\text{inc}}(\bar{r}) = \frac{1}{r} \cdot \exp(i\bar{k}_i \cdot \bar{r}) \quad (4)$$

where $\bar{k}_i = k_{ix}\hat{x} - k_{iy}\hat{y}$ = incident wave vector; and \bar{r} = relative position vector from the radar to any observation point; $|\bar{r}| = r$.

The scattered field from scatterer j at \bar{r}_j and observed at \bar{r} is (Tsang et al. 2000)

$$\psi_{\text{scat}}(\bar{r}, \bar{r}_j) = \frac{s_j(\bar{r}, \hat{k}_i)}{|\bar{r} - \bar{r}_j|} \exp(ik|\bar{r} - \bar{r}_j|) \cdot \psi_{\text{inc}}(\bar{r}) \quad (5)$$

where $s_j = s_j(\bar{r}, \hat{k}_i)$ = scattered amplitude at scatterer j because of an incident wave at \hat{k}_i , observed at \bar{r} . By neglecting the interaction among scatterers, the total scattered field from N scatterer observed at \bar{r} is the summation of the scattered fields from all scatterers

$$\psi_{\text{scat}}(\bar{r}) = \sum_{j=1}^N \frac{s_j(\bar{r}, \hat{k}_i)}{|\bar{r} - \bar{r}_j|} \cdot \exp(ik|\bar{r} - \bar{r}_j|) \cdot \psi_{\text{inc}}(\bar{r}) \quad (6)$$

where $\bar{k}_s = k_{sx}\hat{x} + k_{sy}\hat{y}$ = scattering direction vector; $\bar{k}_s = -\bar{k}_i$ when the radar operates in monostatic mode. Without losing generality, consider the case of single scatterer here. Knowing that $k = \omega/c$ and $\theta = \theta_i = \tan^{-1}(k_{iy}/k_{ix})$, Eq. (5) can be written by

$$\psi_{\text{scat}}(\omega, \theta) = \psi_{\text{scat}}(k, \bar{r}_s) = \frac{s_\theta}{r^2} \cdot \exp\left[i\frac{r}{c}\omega(1 + \cos^2\theta - \sin^2\theta)\right] \quad (7)$$

Eq. (7) is actually a sliced projection of the two-dimensional (2D) Fourier transform (FT) of the domain Ω_s . Unlike the reconstruction algorithms which sum up all projections then perform 2D IFT (plane projection) to obtain the final image, the back-projection algorithm first perform 1D IFT (line projection) to generate subimages. The final image is rendered by summing up all subimages. The center in back-projection images is made coincident with the center of the scatterer by performing a modulation operation in the frequency domain or a convolution operation

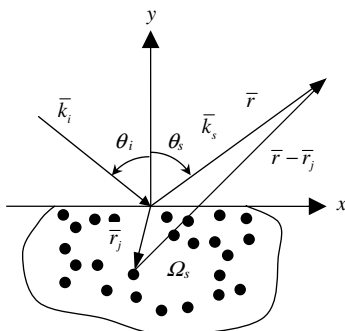


Fig. 4. Scattering of N point scatterers

in time domain. This “shift-back-then-project” scheme coins the name of the algorithm.

The shifting-back step in the back-projection algorithm in frequency domain is performed by applying a ramp filter in which frequency ω_n is shifted back by a carrier frequency ω_c (Desai and Jenkins 1992)

$$\begin{aligned} P(v, \theta) &= \int_{\omega_{\min}}^{\omega_{\max}} d\omega \cdot \psi_{\text{scat}}(\omega - \omega_c, \theta) |\omega - \omega_c| \cdot \exp(-i\omega v) \quad (8a) \\ &= \frac{s_\theta}{r^2} \cdot \int_{\omega_{\min}}^{\omega_{\max}} d\omega \cdot |\omega - \omega_c| \cdot \exp\left[i\frac{r}{c}(\omega - \omega_c)\right] \\ &\quad \times (1 + \cos^2\theta - \sin^2\theta) - i\omega v \quad (8b) \end{aligned}$$

where v = spatial variable of the 1D IFT projection. Translating the local 1D IFT coordinate $[v, P(v, \theta_s)]$ to the global polar coordinate (r, ϕ) indicates that

$$v = r \cos(\phi - \theta_s) \quad (9)$$

Transforming from $P(v, \theta)$ to $P[r \cos(\phi - \theta), \theta]$ is usually associated with upsampling to ensure the quality of image resolution. In other words, $P[r \cos(\phi - \theta), \theta]$ is the interpolated version of $P(v, \theta)$. Computational issues related to such interpolation can be found in the texts on SAR (Carrara et al., 1995; Soumekh 1999).

The back-projection image in polar coordinates is finally obtained by integrating the azimuth angle over the entire inspection range

$$I(r, \phi) = \int_{-\theta_{\text{int}}/2}^{\theta_{\text{int}}/2} d\theta \cdot P(r \cos(\phi - \theta), \theta) \quad (10a)$$

$$\begin{aligned} &= \frac{s_\theta}{r^2} \cdot \int_{-\theta_{\text{int}}/2}^{\theta_{\text{int}}/2} d\theta \int_{\omega_{\min}}^{\omega_{\max}} d\omega \cdot |\omega - \omega_c| \cdot \exp\left[i\frac{r}{c}(\omega - \omega_c)\right] \\ &\quad \times (1 + \cos^2\theta - \sin^2\theta) - i\omega r \cos(\phi - \theta) \quad (10b) \end{aligned}$$

where the polar coordinate variables (r, ϕ) are related to the Cartesian coordinate variables by

$$x = r \cos \phi \quad (11a)$$

$$y = r \sin \phi \quad (11b)$$

Therefore, the image plane $I(x, y) = I(r \cos \phi, r \sin \phi)$ can be reconstructed. Fig. 5 illustrates the processing steps of back-projection algorithms.

From Eq. (10b), it is clear that the final back-projection image is the superposition of subimages generated by using subaperture or subband measurements

$$\begin{aligned} I(r, \phi) &= \sum_{m=1}^M \sum_{n=1}^N \int_{\theta_m}^{\theta_{m+1}} d\theta \int_{\omega_n}^{\omega_{n+1}} d\omega \cdot \tilde{I}_{\text{sub}}(\omega_n, \theta_m) \\ &= \sum_{m=1}^M \sum_{n=1}^N I_{mn}(r, \phi) \quad (12) \end{aligned}$$

where $I_{mn}(r, \phi)$ = subimage processed by using the data of subbandwidth $[\omega_n, \omega_{n+1}]$ and of subaperture range $[\theta_m, \theta_{m+1}]$, suggesting that the aperture (angular) range θ_{int} is divided into M subapertures and the bandwidth into N subbands for processing.

Physical Meaning of the Scattering Signals in Back-Projection Images

In the monostatic mode of radar operation, the scattering signals in back-projection images are proportional to the magnitude of

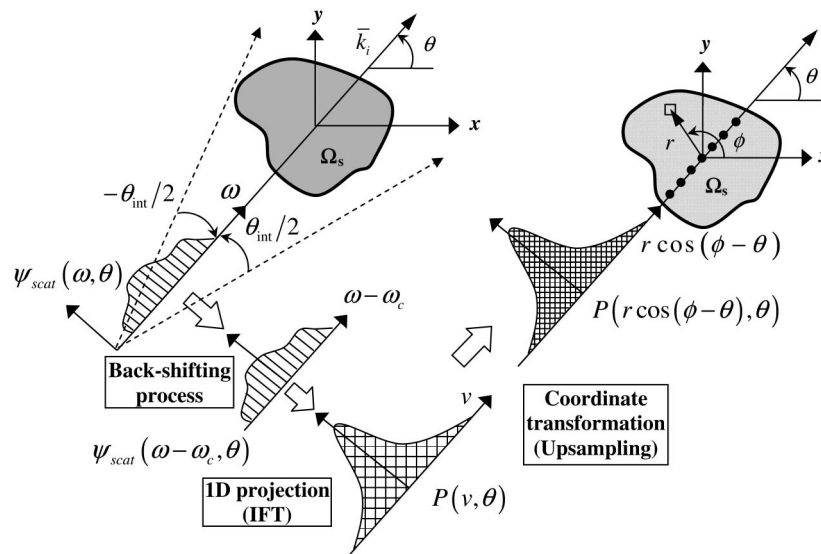


Fig. 5. Processing steps of back-projection algorithms

far-field ISAR measurements. The back-projection processing of ISAR measurements distinguishes the contributions of various scatterers in the physical coordinate system and reconstructs these contributions as the scattering signals in the back-projection image. Therefore, the shape and magnitude of a scattering signal in back-projection images indicate the influence of a scatterer (defect) in the structure. In other words, the presence of defects or damages triggers the scattering effect and is revealed by the back-projection processing.

The back-projection images contains two types of scattering signals; defect scattering signal (or defect signal) and background scattering signal (or background signal). Defect scattering signals are caused by the presence of defects, whereas background scattering signals are attributed to the direction reflection from the surface of the structure. Background scattering signals can be easily identified as long as the information regarding the geometry of the structure is provided beforehand, which is usually the case in field inspection. After excluding background scattering signals, the remaining scattering signals are believed related to the presence (location, size, and orientation) of defects.

Advantages of the Back-Projection Algorithm

The main advantages of the back-projection algorithm include: (1) lower and localized artifact levels than frequency-domain algorithms, (2) easy adjustment to an approximate inverse formula for perturbed problems, (3) readily for parallel computing with limited interprocessor communications, and (4) simple motion compensation by time-shift operation (McCorkle and Rofheart 1996; Nilsson and Anderson 1998).

As a result of the advantages previously mentioned, subimages with different bandwidths and angular ranges can be available before the physical inspection (far-field ISAR measurements) is completed. This enables the technique for different purposes of inspection. For instance, subimages of narrow bandwidths and angular ranges (although poor resolution) are advantageous for preliminary inspections because of their rapid inspection and processing. Final images that use full bandwidth and full angular range data are useful for detailed inspections once a suspicious local area can be determined. The superposing process of subimages provides not only the gradually improved image resolutions (range and cross range), but also the evolution of scattering signals in the image. For example, angular sensitivity of defect scattering signals is revealed

by processing ISAR measurements at each subaperture. It is evident that understanding the pattern (evolution, convergence) of defect scattering signals in back-projection images is beneficial to studying actual defects or damages. Knowledge about the needed frequency bandwidth and angular range for revealing certain types of defects in back-projection images can also be established on the basis of such understanding.

Image Interpretation Processing

Damage assessment of structures is performed on the basis of interpretation of the back-projection images. The presence of defects or damage can be asserted either by (1) discovering suspicious scattering signals in one image after background signals are excluded, or by (2) comparing suspicious images with the one known to be without any defect signals. Either case poses a pattern recognition problem in which the characteristics of defect scattering signals must be studied.

In this paper, the maximum amplitude (local index) and the pattern of back-projection images (global index) are used for quantifying the presence of defects. While the maximum amplitude of a back-projection image locally indicates the significance (size, angular sensitivity) of scattering signals (defect or background), the morphological pattern of a back-projection image captures the global feature of the image. Knowing that the back-projection image of a damaged structure contains defect signals in addition to background signals, the image pattern should be distinguishable from the one of an intact structure. This difference is globally characterized by mathematical morphology using a quantitative index (Euler's number) as a damage indicator. In what follows, these two approaches are to be explained.

Approach I: Maximum Amplitude

Since the presence of defects leads to the appearance of scattering signals in the back-projection images, no defect signals should be expected in the image of an intact structure after excluding background signals. However, in some circumstances, such as the specular dominant case shown in Fig. 6(a), background signals become dominant and cover the defect signal. This is the case when low signal-to-noise ratio (SNR) is encountered, and the maximum amplitude is associated with background signals. Contrarily, in the specular recessive case shown in Fig. 6(b), high SNR can be

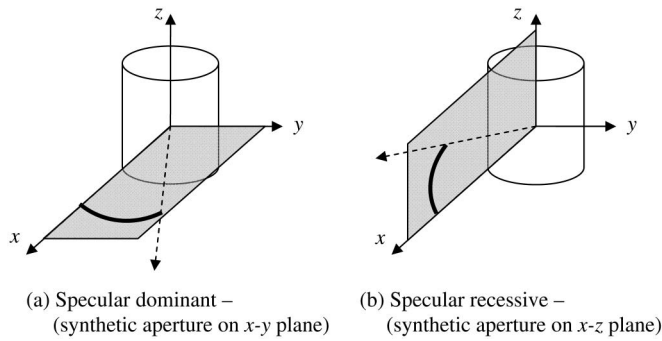


Fig. 6. Specular dominant and recessive modes

expected owing to the alleviation of background signals (noise), and the maximum amplitude is associated with defect signals.

In this paper, the maximum amplitude in the back-projection images can be determined by

$$I_{\max}^i = \max[I^i(x, y) | (x, y) \in \Omega_s] \quad (13a)$$

or

$$I_{\max}^d = \max[I^d(x, y) | (x, y) \in \Omega_s] \quad (13b)$$

or where I_{\max}^i and I_{\max}^d = maximum amplitude in the back-projection images of intact [$I^i(x, y)$] and damaged [$I^d(x, y)$] structures in the domain Ω_s , respectively. (x, y) forms the image plane. Note that the difference in $I^i(x, y)$ and $I^d(x, y)$ is the defect signal. Performance of maximum amplitude index on damage assessment is demonstrated in the “Application” section.

Approach II: Mathematical Morphology

Pattern recognition of the back-projection images is conducted by extracting the features (edges) from the images and by evaluating the features quantitatively by using mathematical morphology.

Global features (e.g., shape of scattering signals) are characterized and quantitatively evaluated by using techniques in mathematical morphology (Shirai 1987; Marchand-Maillet and Sharaiha 2000; Nixon and Aguado 2002). In this paper, the back-projection images are evaluated by mathematical morphology in the following two steps:

1. Feature extraction—The back-projection images are rendered with continuous response levels, in which both background and defect signals are involved. To extract the characteristic shape of a back-projection image, the image is first transformed into a binary image based on a threshold value n_{thv} . Two morphological operations, erosion and dilation, are subsequently applied to the binary image to obtain a feature-extracted version of the original back-projection image. These morphological operations are defined by

$$\varepsilon_K(I) = \{r | K_r \subseteq I(x, y)\} \quad (14)$$

$$\delta_V(I) = \{r | V_r \cap I(x, y) \neq \emptyset\} \quad (15)$$

where $I(x, y)$ = back-projection images; ε_K = erosion operator functioning with the erosion structure K ; K_r = eroded set operating at position r ; δ_V = dilation operator functioning with the dilation structure V ; V_r = dilated set operating at r , and \emptyset = empty set. An eight-node element is adopted for both erosion and dilation structures, as shown in Fig. 7. The feature extraction operation on $I(x, y)$ is performed on the binary version of $I(x, y)$ in this paper, denoted by $I_{BW}(x, y | n_{thv})$. The operation is defined by

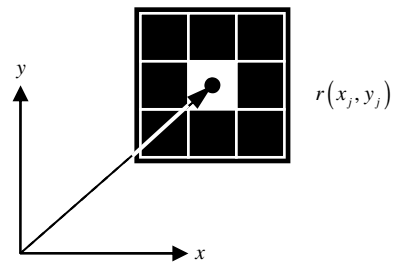


Fig. 7. Eight-node element for morphological operations

$$\hat{I}(x, y | n_{thv}) = \delta_V\{\varepsilon_K[I_{BW}(x, y | n_{thv})]\} \quad (16)$$

where $\hat{I}(x, y | n_{thv})$ = feature-extracted binary image characterized by a threshold value n_{thv} ; n_{thv} = threshold value related to the level of the extracted edge in the image. It is the maximum magnitude level in the image, at which the characteristic shape of the image is preserved.

2. Feature quantification—A quantitative index used in this paper to globally characterize $\hat{I}(x, y | n_{thv})$ is Euler’s number, n_E . The variation of n_E with respect to the incident angle is interesting and investigated here. For each $\hat{I}(x, y | n_{thv})$ obtained at a given incident angle θ , n_E is defined by

$$n_E(\theta | n_{thv}) = n_{obj}(\theta | n_{thv}) - n_{hol}(\theta | n_{thv}) \quad (17)$$

where $n_{obj}(\theta | n_{thv})$ = number of objects in $\hat{I}(x, y | n_{thv})$; and $n_{hol}(\theta | n_{thv})$ = number of holes within the objects in $\hat{I}(x, y | n_{thv})$. With a fixed value of n_{thv} , $n_E(\theta)$ can be obtained.

The presence of damage introduces additional defect signals into back-projection images globally, and changes the maximum amplitude locally. Logically, the presence of a defect creates a defect scattering signal, leading to an increasing n_{hol} . The value of $n_E(\theta)$ is subsequently altered. Given same n_{thv} and same inspection domain Ω_s , the fluctuation of defect scattering signals will create more holes than objects, thus resulting in small $n_E(\theta)$. The purpose of using mathematical morphology is to quantify such change. Additionally, in view of the angular sensitivity of defect signals, it is believed that damage assessment based on single measurement (or image) is unlikely to be reliable. Multiple images (more information) are needed to confirm the speculation on one suspicious image. For this reason, an averaging (low-pass) filter is applied to the $n_E(\theta)$ curve, which is defined by

$$n_E^f(\theta) = \sum_{\theta = -\theta_{m/2}}^{\theta_{m/2}} \frac{n_E(\theta)}{L} \quad (18)$$

where $n_E^f(\theta)$ = filtered n_E curve; and L = length of the filter (data points used in the filter). The purpose of this filter is to remove local fluctuations from the original n_E curve in order to (1) avoid false alarms at local level and (2) obtain globally consistent results. Additionally, the length of the filter suggests the required amount of angular measurements. The length of the filter also relies on the resolution of the image. For high resolution images, small L values are expected.

Application

The proposed damage assessment method is validated using the far-field ISAR measurements of two GFRP-confined concrete cylinder specimens. These specimens are further subjected to physical radar measurements in the radar facility at the Massachusetts Institute of

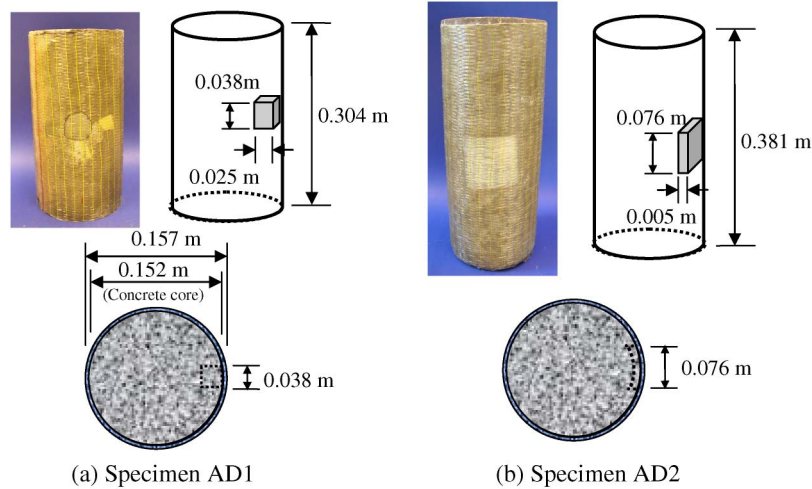


Fig. 8. Two artificially damaged GFRP-concrete specimens

Technology (MIT) Lincoln Laboratory. Collected far-field ISAR measurements are processed by the image reconstruction algorithm to render back-projection images. The reconstructed images are analyzed by using both a local index (maximum amplitude) and a global index (Euler's number) for damage assessment.

In the following section, a description of the specimens and their far-field ISAR measurements are provided. Physical inspection, numerical processing, and pattern recognition by using radar measurements from the GFRP-confined concrete specimens are also explained.

Description of Laboratory Specimens

Two GFRP-confined concrete cylinder specimens are artificially damaged by inserting artificial anomalies (Styrofoam piece and sheet) at the interface region between GFRP sheet and the concrete core. Dimensions of the specimens and defect configuration are illustrated in Fig. 8(a) and 8(b), in which Fig. 8(a) shows Specimen AD1 with a cubicle-like defect, and Fig. 8(b) shows Specimen AD2 with a delamination-type defect. Both defects are inserted

Table 1. Description of GFRP-Concrete Cylinder Specimens

Property	Description
Size of the concrete cylinder	Diameter: 15.2 cm/height: 30.4 cm and 38.1 cm
Thickness of GFRP-epoxy layer	0.25 cm
Cement type	Portland type I
Mix ratio of concrete (by weight)	Water:cement:sand:aggregate = 0.45:1:2.52:3.21
Curing duration	28 days
GFRP brand	Tyfo SEH-51A (by Fyfe Co. LLC)
Epoxy brand	Tyfo S Epoxy (by Fyfe Co. LLC)
Volumetric ratio of GFRP-epoxy layer	0.645:0.355
Dielectric constant (ϵ_r') and loss factor (ϵ_r'') of concrete at 10 GHz	5.69 0.62
Dielectric constant (ϵ_r') and loss factor (ϵ_r'') of GFRP at 10 GHz	5.004 0.112
Dielectric constant (ϵ_r') and loss factor (ϵ_r'') of Styrofoam	1 0

approximately at the midheight of the specimens. Material properties of the GFRP-concrete specimens are summarized in Table 1. These specimens were manufactured and subjected to far-field ISAR measurements in a laboratory environment.

Physical Inspection

Monostatic far-field ISAR measurements of the GFRP-concrete specimens were conducted at the MIT Lincoln Laboratory using the Compact RCS (radar cross section)/Antenna Range facility designed for performing far-field measurements. Measurements were collected in specular recessive configuration, as shown in Fig. 6(b), in which the specular return is only significant when the axis of the cylinder is perpendicular to line-of-sight of the radar. This facility can achieve high SNR for a large frequency bandwidth ranging from 0.7 GHz to 100 GHz. SNR is enhanced by the coherent, wide bandwidth measurements. The radar system is capable of producing a far-field condition with a 20-m quiet zone, different antenna radiation patterns, and full polarimetric RCS measurements. Far-field ISAR measurements were conducted in X-band (8 GHz to 12 GHz) at an interval of 0.02 GHz. Time-harmonic continuous EM waves of both HH (horizontally polarized transmitting and receiving) and VV (vertically polarized transmitting and receiving) polarization were used (Kong 2000). The angular range of inspection was 60° (30° on each side) with an interval of 0.2° . Accomplishing the physical inspection of the GFRP-confined concrete specimens provided the frequency-angle data. In this paper, three data sets are reported; (1) intact side of Specimen AD1, (2) damaged side of Specimen AD1, and (3) damaged side of Specimen AD2, which are illustrated in Fig. 9. The intact side of Specimen AD2 was not measured because of the time constraint

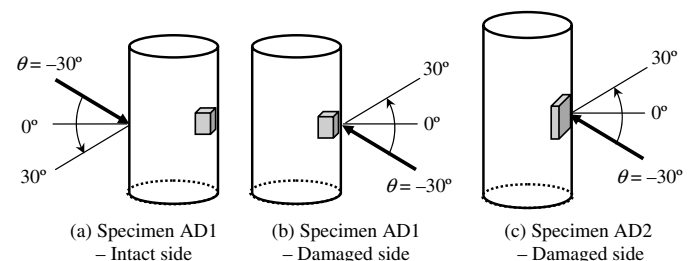


Fig. 9. Three frequency-angle data sets of the far-field ISAR measurements

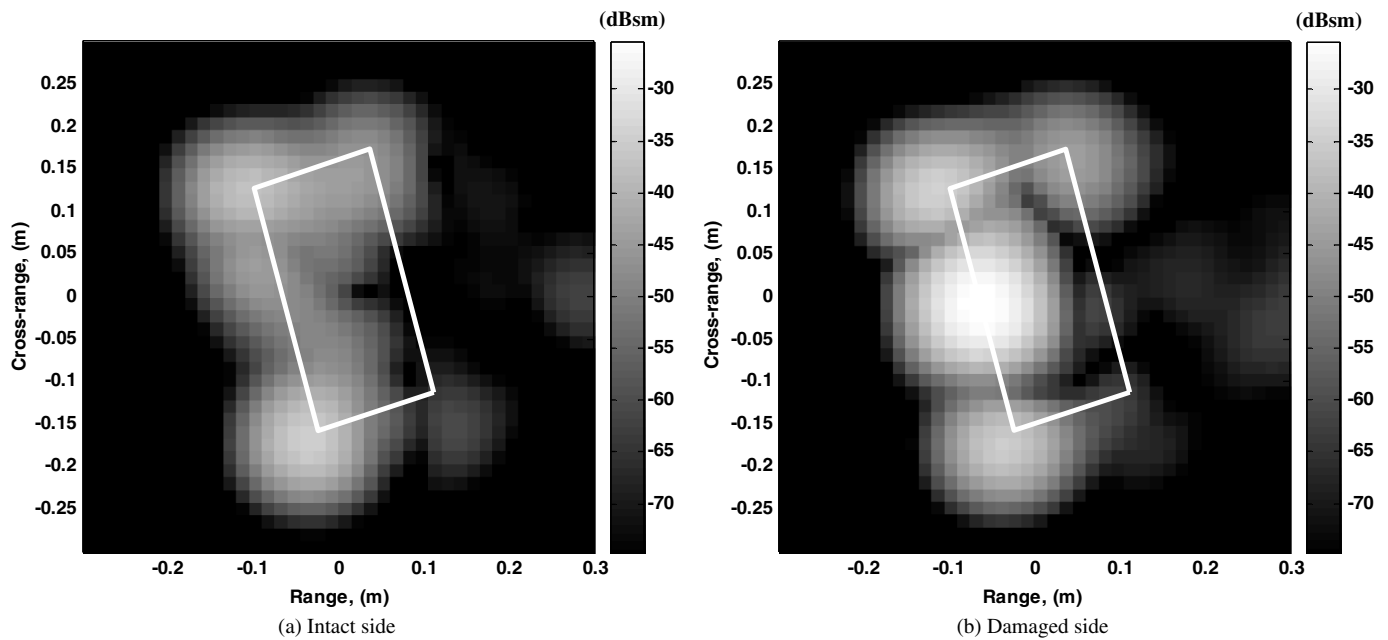


Fig. 10. Reconstructed images of the intact and damaged sides of Specimen AD1—HH polarization ($\theta = -15^\circ$)

in the experimental work at the MIT Lincoln Laboratory. Additionally, measurements and their reconstructed image (Fig. 10) on the intact side of Specimen AD1 have provided key features of the specimen and, therefore, can be used as a basis for comparing intact and damaged specimens in this study.

Numerical Processing

Collected frequency-angle data (far-field ISAR measurements) of Specimens AD1 and AD2 with full frequency bandwidth (8 GHz to 12 GHz) were processed by the image reconstruction algorithm to obtain back-projection images (in-depth profile), as shown in Figs. 11–13. Both HH and VV polarized signals were used. In these images, the specimens were tilted at 15° to alleviate

the impact of specular returns. The response level in these images ranged from -25 dBsm (decibel per square meter) to -75 dBsm. With the full bandwidth, the range (x-axis) and cross range (y-axis) resolutions were 0.0372 m (1.46 in) and 0.0401 m (1.58 in), respectively.

In Fig. 10(a), two background scattering signals caused by the edge reflection of Specimen AD1 are observed. In Fig. 10(b), the presence of the artificial defect is revealed by a strong defect signal in the middle of Specimen AD1 by using HH polarized radar signals. The center of the defect signal coincides with the center of where the Styrofoam defect is physically inserted. Same observation is found by using VV polarized radar signals, as shown in Figs. 11(a) and 11(b).

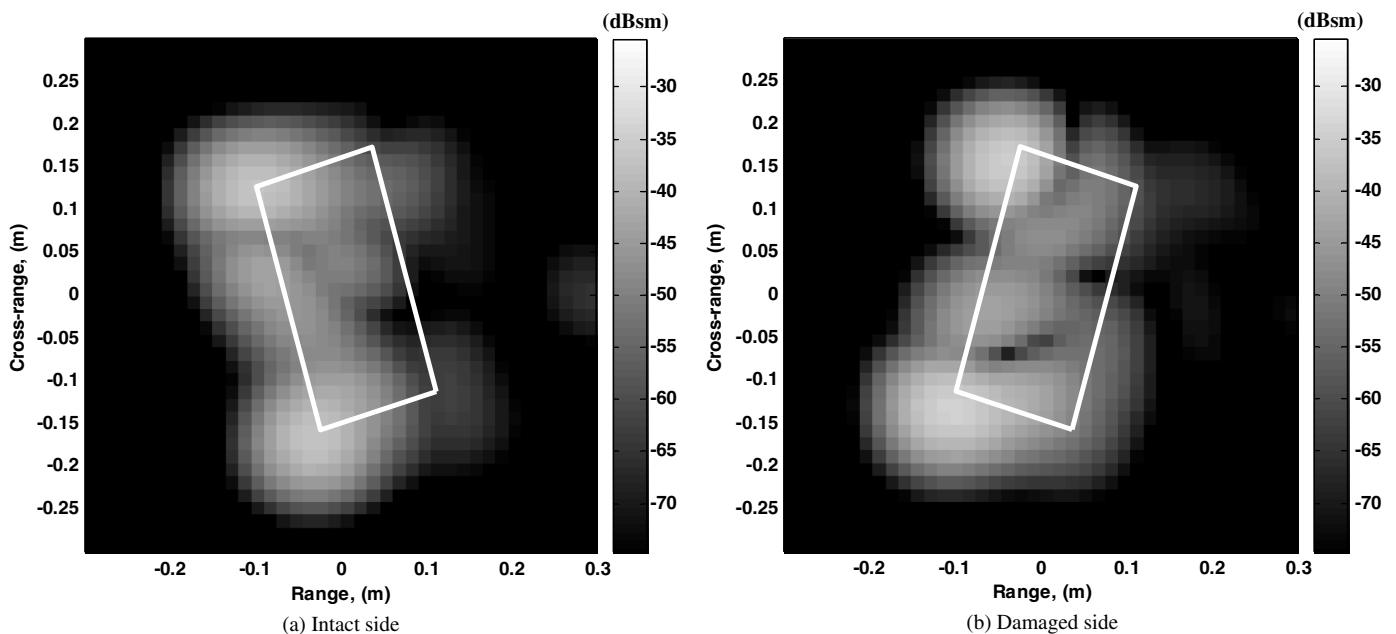


Fig. 11. Reconstructed images of the intact and damaged sides of Specimen AD1—VV polarization ($\theta = -15^\circ$)

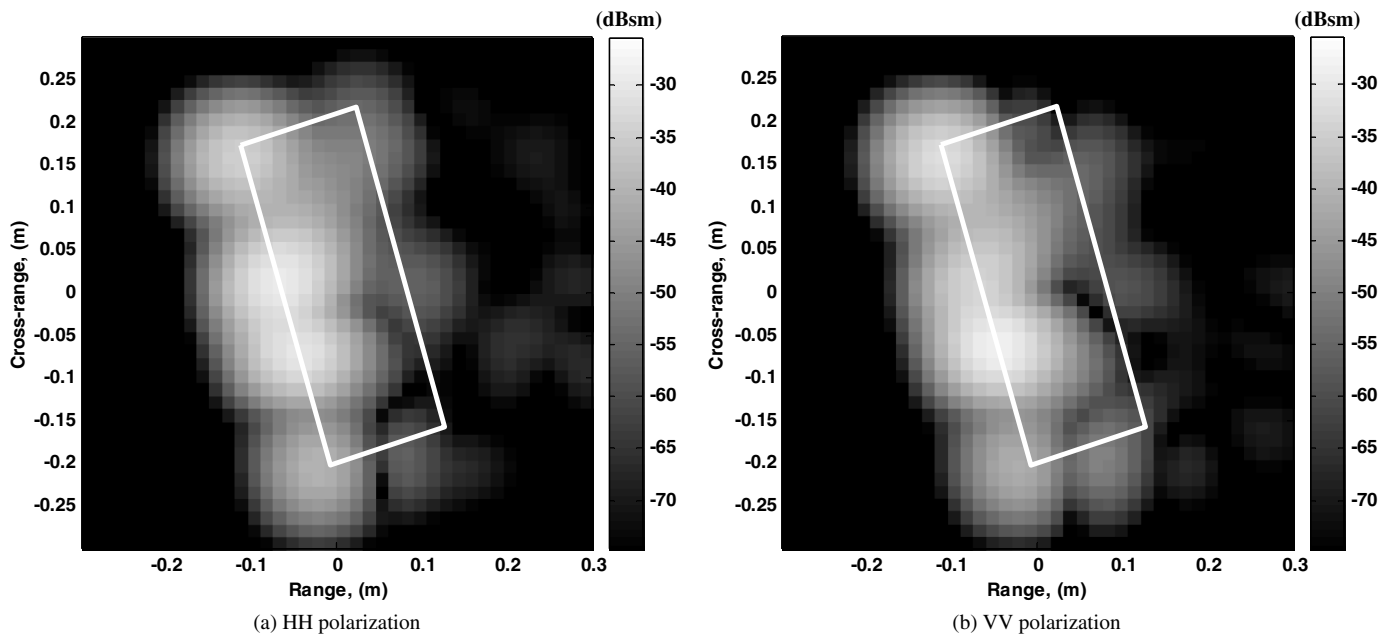


Fig. 12. Reconstructed images of the damaged side of Specimen AD2 ($\theta = -15^\circ$)

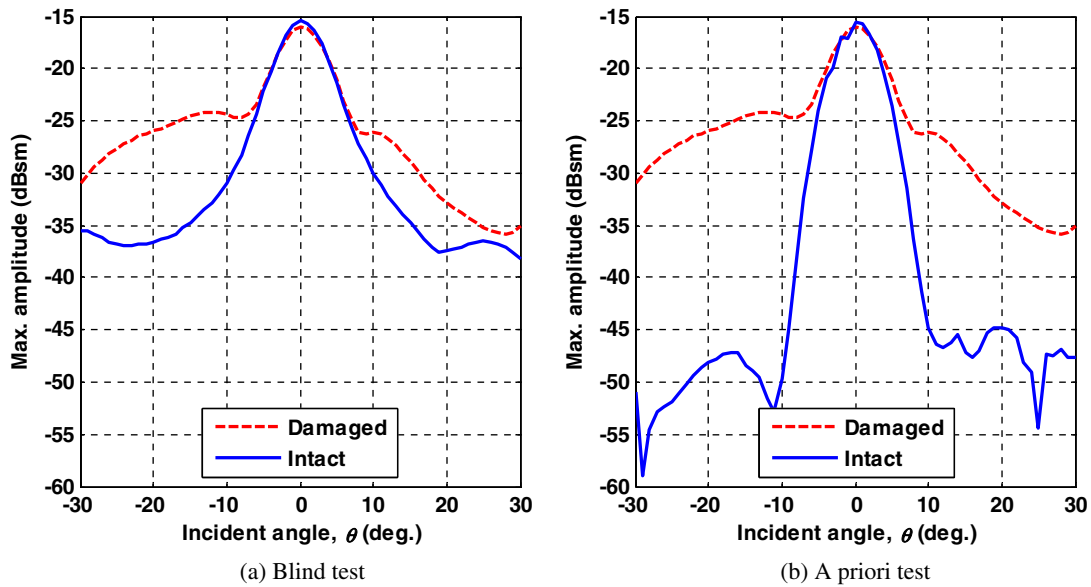


Fig. 13. Maximum amplitudes of the back-projection images of Specimen AD1

In Fig. 12, processed back-projection images (HH and VV polarizations) of Specimen AD2 even reveal the detailed information of a delamination defect. Within the region where the defect scattering signal is found, two distinguishable peaks are discovered. The locations of these two peaks correspond to where the two edges of the delamination defect are inside Specimen AD2.

To explain the results in Figs. 10–12, comparison among the minimum wavelength, image resolutions, and the characteristic length of two defects is provided in Table 2. It is known that the size (characteristic length l_{ch}) of defects must be greater than the minimum wavelength λ_{min} in order to trigger the scattering effect (to be detectable); but, as demonstrated in this example, l_{ch} must be sufficiently greater $\max(\rho_r, \rho_{xv})$ so as to be recognizable in the reconstructed images. In Table 2, the characteristic length of the cubiclike defect in Specimen AD1 is only slightly greater than the

maximum resolution in the image. Therefore, details of the defect are not clearly recognizable. Contrarily, the l_{ch} of the delamination defect is much greater than the maximum resolution, suggesting the detectability of such defect. From the results in Figs. 10–12, the

Table 2. Comparison of Signal Wavelength, Image Resolution, and Characteristic Length of Defects

Minimum wavelength, λ_{min} (at 12 GHz)	Image resolutions at full bandwidth	Characteristic length of defects, l_{ch}
In air: 0.0125 m	ρ_r : 0.0372 m (range or x)	AD1: 0.0455 m
In concrete: 0.0112 m (dielectric constant = 5)	ρ_{xv} : 0.0401 m (cross-range or y)	AD2: 0.0762 m

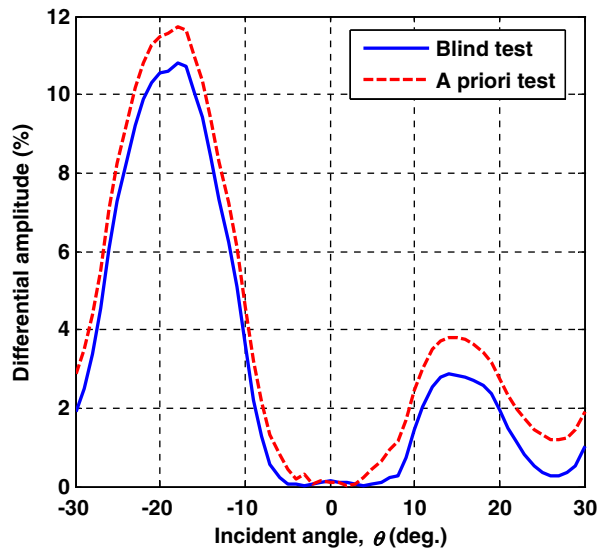


Fig. 14. Differential amplitudes ΔA in both blind test and a priori test from Fig. 13

presence of the artificial defect has been successfully revealed in the back-projection images.

Pattern Recognition

On applying the method for damage assessment in this section, only the back-projection images of Specimen AD1 are used for the reason that both intact and damaged responses of the specimen are available for direct comparison.

Local Index—Maximum Amplitude

In this approach, identifying background signals is important (in order to exclude them), and it is interesting to know how influential background signals could be on the result. Maximum amplitudes are extracted from the back-projection images in two scenarios; (1) including background signals (blind test), and (2) excluding background signals (a priori test). Evaluating a back-projection image without excluding background signals is a blind test, from which the overall maximum amplitude is obtained. Excluding

background signals requires a priori knowledge about the structure. Figs. 13(a) and 13(b) show the maximum amplitudes of back-projection images produced from the intact and damaged sides of Specimen AD1 in both scenarios.

In Figs. 13(a) and 13(b), two curves of maximum amplitude are presented. As previously mentioned in this paper, the presence of defects introduces defect signals in the reconstructed images. The difference between the intact and damaged maximum amplitude curves indicates the degree of detectability. In this example, it is observed that the defect signal is detectable in two angular regions, $\theta \in [-30^\circ, -7^\circ]$ and $\theta \in [7^\circ, 30^\circ]$, in blind test scenario in Fig. 13(a). Two similar regions are also found in Fig. 13(b) where background signals are excluded, but with better detectability because of the significant separation between the curves. In the angular region $\theta \in (-7^\circ, 7^\circ)$, specular effects are dominant, and the difference is not distinguishable.

Differential amplitude between maximum amplitude curves is also calculated for both blind test and a priori test scenarios, as shown in Fig. 14. The differential amplitude, ΔA , is determined by

$$\Delta A = \frac{A_d - A_i}{A_i} \quad (19)$$

where A_d = damage curve; and A_i = intact curve in Fig. 13. The blind test is performed by taking the absolute maximum scattering response of the image (including the scattering responses from the background), while a priori test is conducted by taking the relative maximum scattering response centered at the possible defect location (excluding the scattering responses from the background). In Fig. 14, ΔA is shown in percentage, whose pattern demonstrates the sensitivity and effectiveness of incident angle on damage assessment. It is found that, in the case of Specimen AD1, oblique incident scheme provides a robust performance with slight influence from the background scattering signals. Meanwhile, optimal incident angle can also be determined by ΔA ; the optimal incident angle is approximately 15° in this example. It is also observed that the maximum values of ΔA on two sides are different, while their almost-identical location ($\sim +15^\circ$ and $\sim -15^\circ$) confirms the symmetrical feature of the defect (the defect produces symmetric scattering). Conclusions are drawn from the example presented in this section.

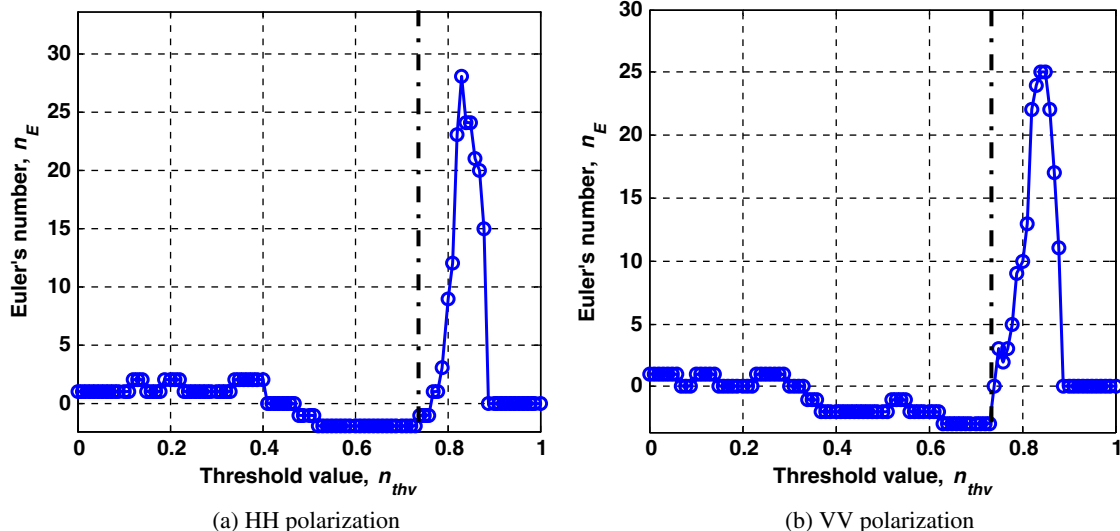


Fig. 15. Variation of n_E with respect to n_{thv} of the damaged-side images of Specimen AD1

Global Index—Mathematical Morphology

In generating the feature-extracted images $\hat{I}(x, y|n_{thv})$ the value of n_{thv} must be determined. The value of n_{thv} is decided when the variation of Euler's number n_E is at critical stage. When small n_{thv} values are chosen, all or most of the signals are preserved, leading to a feature-extracted image $\hat{I}(x, y|n_{thv})$ dominated by low amplitude signals. When large n_{thv} values are chosen, $\hat{I}(x, y|n_{thv})$ will be dominated by high amplitude signals. Consequently, the computed Euler's number n_E in these two extreme cases does not represent/reflect the main feature of the image. To avoid the use of misleading n_{thv} , the pattern of n_E is provided, as shown in Figs. 15 and 16, in which n_{thv} is normalized to the maximum amplitude of $\hat{I}(x, y|n_{thv})$. Fig. 15 shows the variation of n_E versus n_{thv} computed from the intact-side back-projection images of Specimen AD1. Fig. 17(a) is produced from Fig. 10(a) and Fig. 17(b) from Fig. 11(a). In Figs. 15(a) and 15(b), fluctuation of n_E in the region where n_{thv} is small ($0 < n_{thv} < 0.4$) is attributed to background signals, while in another region of large n_{thv} ($0.73 < n_{thv} < 1$) the fluctuation of n_E is caused by the disturbance of high amplitude signals. In both regions, the computed n_E does not represent the main feature of the image. To avoid using misleading values of n_E , the critical n_{thv} should be determined as the maximum n_{thv} outside these two regions. As indicated in Figs. 15(a) and 15(b), critical n_{thv} is 0.81 for the images by using both HH and VV polarized signals. In Figs. 16(a) and 16(b), critical n_{thv} is 0.73.

Fig. 16 shows the reconstructed back-projection images $I(x, y)$ and their feature-extracted version $\hat{I}(x, y|n_{thv})$ of Specimen AD1 by

using HH polarized signals at full bandwidth. With the selection of critical n_{thv} , the generated $\hat{I}(x, y|n_{thv})$ captures the main feature of the original back-projection images $I(x, y)$. The feature-extracted images using VV polarized signals also provide similar result and are not repeatedly shown here. The Euler's number of the intact-side image $\hat{I}(x, y|n_{thv} = 0.81)$ is $n_E = -1$. For the damaged-side image $\hat{I}(x, y|n_{thv} = 0.73)$, $n_E = -2$.

Following the same procedure described above, $\hat{I}(x, y|n_{thv})$ can be produced for other incident angles, resulting in the intact-side and damaged-side curves $n_E(\theta)$ of Specimen AD1, as shown in Fig. 18. The $n_E(\theta)$ curves in Fig. 18 demonstrate the sensitivity and effectiveness of incident angle with respect to the damage indication by using Euler's number. Since the scattering caused by defects is angle-dependent, evaluating the structure by using images at several incident angles is needed. This leads to the application of an averaging filter to obtain $n_E^f(\theta)$ curves.

Fig. 19 shows the $n_E^f(\theta)$ by using a filter length (data points) of $L = 3$. In Fig. 19, the filtering processing produces a clear separation between the intact-side and damaged-side $n_E(\theta)$ curves, except in the specular dominant region [$\theta \in (-10^\circ, 10^\circ)$]. The values of $n_E(\theta)$ of the intact-side images are in general greater than the ones of the damaged-side images since the presence of defect signals creates more holes in the images, resulting in smaller values of $n_E(\theta)$. In addition, the filter length is related to the required amount of angular measurements for achieving a globally consistent assessment. In this case, at least three angular

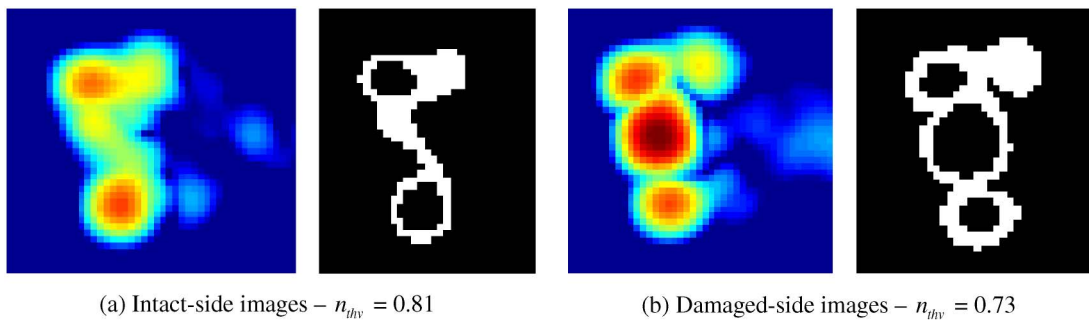


Fig. 16. Back-projection images and their feature-extracted version of Specimen AD1 (HH polarization, full bandwidth, $\theta = -15^\circ$)

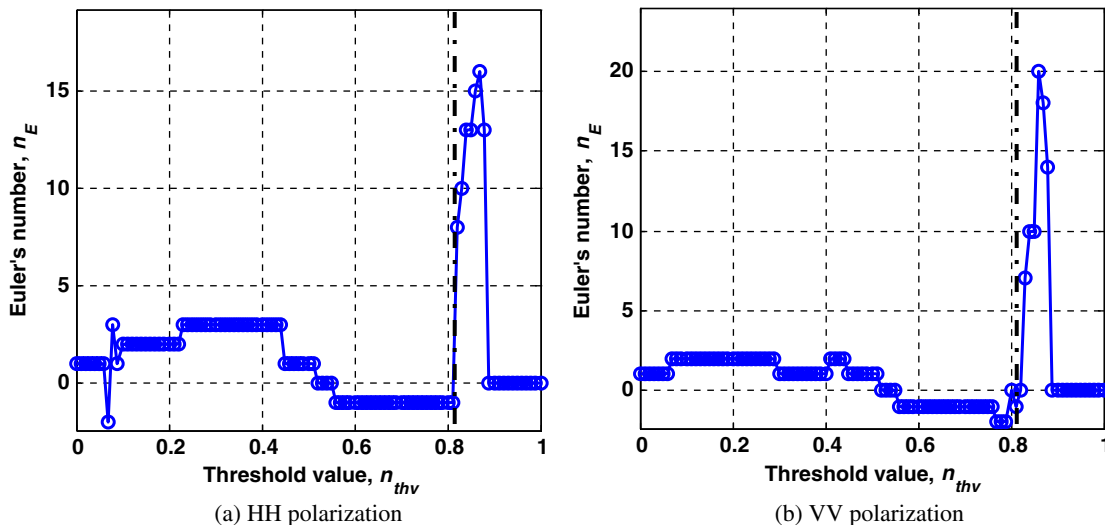


Fig. 17. Variation of n_E with respect to n_{thv} of the intact-side images of Specimen AD1

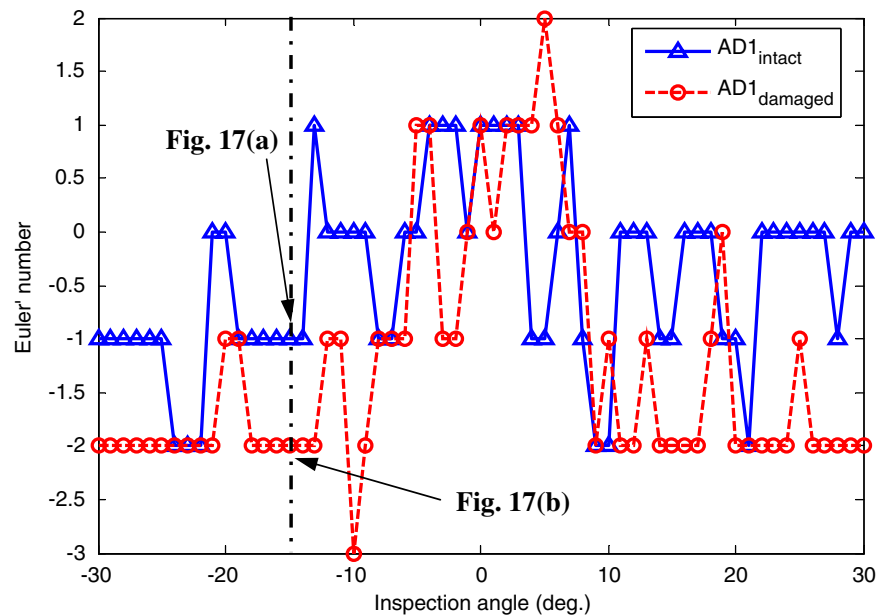


Fig. 18. Original $n_E(\theta)$ curves of the intact and damaged surfaces of Specimen AD1

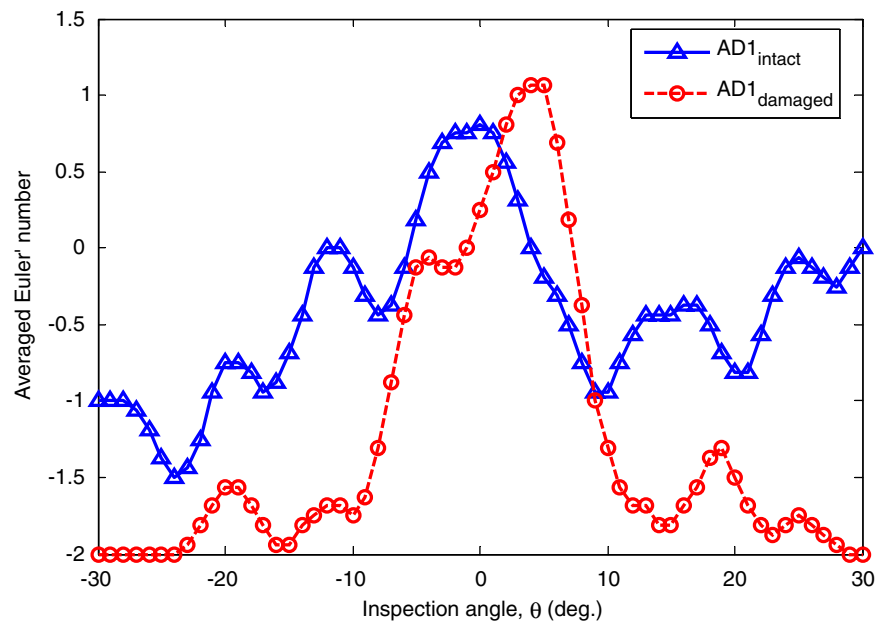


Fig. 19. Filtered n_E curves of the intact and damaged surfaces of Specimen AD1

measurements (data points) are needed for each comparison between the images of intact and damaged structures.

Conclusions

This paper proposes a method for damage assessment of multilayer composite systems using far-field radar measurements. As an example of multilayer composite systems, GFRP-concrete cylinders with an artificial defect were manufactured and subjected to laboratory radar measurements for validation. The presence of an artificial defect is visually revealed in the reconstructed back-projection images (Figs. 11–13) and is quantitatively evaluated with a local index (Figs. 14 and 17) and a global index (Figs. 18

and 19) defined in this paper. Findings from the validation of the method are summarized in the following.

1. Effectiveness of incident angle on damage assessment is affected by the measurement scheme. In the specular recessive scheme shown in Fig. 6(b), background signals dominate the total response, making defect signals undetectable. Relevant inspection scheme must be chosen to alleviate the impact of background signals in the method.
2. The processing of far-field radar measurements by using the back-projection algorithm shows promising results by successfully discovering the presence of an artificial defect in reconstructed back-projection images (Figs. 11–13). However, assertion on their presence should be made based on the images at several incident angles.

3. As evaluated by using a local index (maximum amplitude), it is confirmed that detectability of defects is angle-dependent. A defect or cracking can be more detectable in some angular ranges than in others. With a priori knowledge about background signals, detectability can be improved. Additionally, the shape of the maximum amplitude curve of the intact side indicates the pattern of background signals.
4. As evaluated by using a global index (Euler's number), the presence of a defect results in the fluctuation of defect scattering signals in the images, creating more holes in the images and leading to a smaller $n_E(\theta)$.
5. In producing the feature-extracted images of structures, the critical threshold value must be used. This step is important to reliably render a representative version of the original back-projection image for the image quantification by using Euler's number.
6. Pattern recognition of the reconstructed images by using morphological operations further provides a quantitative evaluation tool for distinguishing the responses of intact and damaged structures.
7. Effectiveness of incident angle on damage assessment is affected by the measurement scheme. In the specular recessive scheme shown in Fig. 6(b), background signals dominate the total response, making defect signals undetectable. This is the case of $\theta \in (-7^\circ, 7^\circ)$ in Figs. 13(a) and 13(b).
8. Detectability of defects is sensitive to the selection of incident angles. A defect or damage is more detectable in some ranges of incident angle than in others.
9. With a priori knowledge about background signals, detectability can be improved, although the blind test result already provides a satisfactory performance, as shown in Fig. 14.
10. The shape of the maximum amplitude curve of the intact side indicates the pattern of background signals.
11. Optimal incident angles can be determined by using the concept of differential amplitude ΔA . Detailed features of defect can be observed by the distribution of ΔA .

Ongoing research topics for the future development of the proposed method include the study of other types of artificial defects, such as compressive cracking of concrete, other elements for morphological operations, sensitivity of morphological indices to the inspection angle, and the ability of the method to inversely reconstruct the orientation and magnitude of defects.

Acknowledgments

The experimental work in this paper was partially supported by the MIT Lincoln Laboratory through Grant Advanced Concept Committee (ACC)-376 with the assistance of D. Blejer at the MIT Lincoln Laboratory, whose efforts are gratefully acknowledged. The author would like to thank Dr. T. M. Grzegorzczak from Delpsi, LLC, and the late Prof. Jin Au Kong at MIT for their valuable suggestions made on this work. This work was also partially supported by the National Science Foundation (NSF) through Grant CMS-0324607 during the author's doctoral study under the supervision of Prof. O. Buyukozturk at MIT. The financial support from NSF is sincerely appreciated.

References

- Akuthota, B., Hughes, D., Zoughi, R., Myers, J., and Nanni, A. (2004). "Near-field microwave detection of disband in carbon fiber reinforced polymer composites used for strengthening cement-based structures and disbond repair verification." *J. Mater. Civ. Eng.*, 16(6), 540–546.

- Al-Qadi, I. L., Hazim, O. A., and Riad, S. M. (1995). "Dielectric properties of Portland cement concrete at low radio frequencies." *J. Mater. Civ. Eng.*, 7(3), 192–198.
- Arunachlam, K., Melapudi, V. R., Upda, L., and Upda, S. S. (2006). "Microwave NDT of cement-based materials using far-field reflection coefficients." *NDT&E Int.*, 39(7), 585–593.
- Au, C., and Buyukozturk, O. (2005). "Effect of fiber orientation and ply mix on fiber reinforced polymer-confined concrete." *J. Compos. Constr.*, 9(5), 397–407.
- Bechly, M. E., and Clausen, P. D. (1997). "Structural design of a composite wind turbine blade using finite element analysis." *Compos. Struct.*, 63(3), 639–646.
- Binda, L., Lenzi, G., and Saisi, A. (1998). "NDE of masonry structures: Use of radar tests for the characterization of stone masonries." *NDT&E Int.*, 31(6), 411–419.
- Blitz, J. (1997). *Electrical and magnetic methods of non-destructive testing*, Chapman & Hall, New York.
- Bois, K. J., Benally, A. D., and Zoughi, R. (2000). "Microwave near-field reflection properties analysis of concrete for material content determination." *IEEE Trans. Instrum. Meas.*, 49(1), 49–55.
- Buyukozturk, O., and Rhim, H. C. (1995). "Radar measurements of concrete for nondestructive evaluation of dams." *Proc. SPIE on NDE of Aging Structs. Dams*, 2457, 168–174.
- Carrara, W. G., Goodman, R. S., and Majewski, R. M. (1995). *Spotlight synthetic aperture radar—Signal processing algorithms*, Artech House, Boston.
- Chambers, A. R., Earl, J. S., Squires, C. A., and Suhot, M. A. (2006). "The effect of voids on the flexural fatigue performance of unidirectional carbon fibre composites developed for wind turbine applications." *Int. J. Fatigue*, 28(10), 1389–1398.
- Chen, H.-P., and Leib, D. (1993). "Dynamic delamination growth in laminated composite structures." *Compos. Sci. Technol.*, 46(4), 325–333.
- Correia, J. R., Branco, F. A., and Ferreira, J. (2009). "GFRP—concrete hybrid cross-sections for floors of buildings." *Eng. Struct.*, 31(6), 1331–1343.
- Desai, M. D., and Jenkins, W. K. (1992). "Convolution backprojection image reconstruction for spotlight mode synthetic aperture radar." *IEEE Trans. Image Process.*, 1(4), 505–517.
- Dobрила, P., and Premrov, M. (2003). "Reinforcing methods for composite timber frame-fiberboard wall panels." *Eng. Struct.*, 25(11), 1369–1376.
- Farrar, C. R., Darling, T. W., Migliori, A., and Baker, W. E. (1999). "Microwave interferometers for non-contact vibration measurements on large structures." *Mech. Syst. Signal Process.*, 13(2), 241–253.
- Feng, M. Q., De Flaviis, F., and Kim, Y. J. (2002). "Use of microwave for damage detection of fiber reinforced polymer-wrapped concrete structures." *J. Eng. Mech.*, 128(2), 172–183.
- Forde, M. C., McCann, D. M., Clark, M. R., Broughton, K. J., Fenning, P. J., and Brown, A. (1999). "Radar measurement of bridge scour." *NDT&E Int.*, 32(8), 481–492.
- Grande, E., Milani, G., and Sacco, E. (2008). "Modelling and analysis of FRP-strengthened masonry panels." *Eng. Struct.*, 30(7), 1842–1860.
- Hameed, Z., Hong, Y. S., Cho, Y. M., Ahn, S. H., and Song, C. K. (2009). "Condition monitoring and fault detection of wind turbines and related algorithms: A review." *Renew. Sustain. Energ. Rev.*, 13(1), 1–39.
- Janke, L., Czaderski, C., Ruth, J., and Motavalli, M. (2009). "Experiments on the residual load-bearing capacity of prestressed confined concrete columns." *Eng. Struct.*, 31(10), 2247–2256.
- Kak, A. C., and Slaney, M. (1999). *Principles of computerized tomographic imaging*, IEEE Press, New York.
- Keller, T., and Schollmayer, M. (2004). "Plate bending behavior of a pultruded GFRP bridge deck system." *Compos. Struct.*, 64(3–4), 285–295.
- Kensche, C. W. (2006). "Fatigue of composites for wind turbines." *Int. J. Fatigue*, 28(10), 1363–1374.
- Kim, Y. J., Jofre, L., De Flaviis, F., and Feng, M. Q. (2004). "Microwave subsurface imaging technology for damage detection." *J. Eng. Mech.*, 130(7), 858–866.
- Klysz, G., Balayssac, J.-P., and Laurens, S. (2004). "Spectral analysis of radar surface waves for non-destructive evaluation of cover concrete." *NDT&E Int.*, 37(3), 221–227.

- Kong, J. A. (2000). *Electromagnetic wave theory*, EMW Publishing, Cambridge, MA.
- Kumar, P., Chandrashekhara, K., and Nanni, A. (2004). "Structural performance of a FRP bridge deck." *Constr. Build. Mater.*, 18(1), 35–47.
- Kurita, K., Oyado, M., Tanaka, H., and Tottori, S. (2009). "Active infrared thermographic inspection technique for elevated concrete structures using remote heating system." *Infrared Phys. Technol.*, 52(5), 208–213.
- Lam, K. Y., Zong, Z., and Wang, Q. X. (2003). "Dynamic response of a laminated pipeline on the seabed subjected to underwater shock." *Composites, Part B*, 34(1), 59–66.
- Li, J., and Liu, C. (2001). "Noncontact detection of air voids under glass epoxy jackets using a microwave system." *Subsurface Sens. Technol. Appl.*, 2(4), 411–423.
- Lissel, S. L., and Gayevoy, A. (2003). "The use of FRPs in masonry: A state of the art review." *Proc. Int. Conf. on the Performance of Construction Materials*, Cairo, Egypt, 1243–1252.
- Maierhofer, C., Brink, A., Rollig, M., and Wiggenhauser, H. (2003). "Detection of shallow voids in concrete structures with impulse thermography and radar." *NDT&E Int.*, 36(4), 257–263.
- Maierhofer, C., Krause, M., and Wiggenhauser, H. (1998). "Non-destructive investigation of slucies using radar and ultrasonic impulse echo." *NDT&E Int.*, 31(6), 421–427.
- Maierhofer, C., and Leipold, S. (2001). "Radar investigation of masonry structures." *NDT&E Int.*, 34(2), 139–147.
- Marchand-Maillet, S., and Sharaiha, Y. M. (2000). *Binary digital image processing*, Academic Press, San Diego.
- Marín, J. C., Barroso, A., París, F., and Cañas, J. (2008). "Study of damage and repair of blades of a 300 kW wind turbine." *Energy*, 33(7), 1068–1083.
- McCorkle, J., and Rofheart, M. (1996). "An order $n^2 - \log n$ backprojection algorithm for focusing wide-angle wide-bandwidth arbitrary-motion synthetic aperture radar." *Proc. of SPIE*, 2747, 25–36.
- McGeorge, D., Echtermeyer, A. T., Leong, K. H., Melve, B., Robinson, M., and Fischer, K. P. (2009). "Repair of floating offshore units using bonded fibre composite materials." *Composites Part A*, 40(9), 1364–1380.
- Meier, U. (1995). "Strengthening of structures using carbon fibre/epoxy composites." *Constr. Build. Mater.*, 9(6), 341–353.
- Millard, S. G., Bungey, J. H., Thomas, C., Soutos, M. N., Shaw, M. R., and Patterson, A. (1998). "Assessing bridge pier scour by radar." *NDT&E Int.*, 31(4), 251–258.
- Nadakuduti, J., Chen, G., and Zoughi, R. (2006). "Semiempirical electromagnetic modeling of crack detection and sizing in cement-based materials using near-field microwave methods." *IEEE Trans. Instrum. Meas.*, 55(2), 588–597.
- Nilsson, S., and Andersson, L.-E. (1998). "Application of fast back-projection techniques for some inverse problems of synthetic aperture radar." *Proc. of SPIE* 3370, 62–72, Orlando, FL.
- Nixon, M. S., and Aguado, A. S. (2002). *Feature extraction and image processing*, Newnes, Oxford, UK.
- Pieraccini, M., et al. (2004). "Remote sensing of building structural displacements using a microwave interferometer with imaging capability." *NDT&E Int.*, 37(7), 545–550.
- Qaddoumi, N., Ranu, E., McColskey, J. D., Mirshahi, R., and Zoughi, R. (2000). "Microwave detection of stress-induced fatigue cracks in steel and potential for crack opening determination." *Res. Nondestr. Eval.*, 12, 87–103.
- Radford, D. W., Van Goethem, D., Gutkowski, R. M., and Peterson, M. L. (2002). "Composite repair of timber structures." *Constr. Build. Mater.*, 16(7), 417–425.
- Rahami, H., and Hutchinson, A. (2001). "Concrete beams strengthened with externally bonded FRP plates." *J. Compos. Constr.*, 5(1), 44–56.
- Rhim, H. C., and Buyukozturk, O. (2000). "Wideband microwave imaging of concrete for nondestructive testing." *J. Struct. Eng.*, 126(12), 1451–1457.
- Saadatmanesh, H., and Ehsani, M. R. (1991). "RC beams strengthened with FRP plates I: Experimental study." *J. Struct. Eng.*, 117(11), 3417–3433.
- Shaw, M. R., Millard, S. G., Molyneaux, T. C. K., Taylor, M. J., and Bungey, J. H. (2005). "Location of steel reinforcement in concrete using ground penetrating radar and neural networks." *NDT&E Int.*, 38(3), 203–212.
- Sheikh, S. A., and Yau, G. (2002). "Seismic behaviour of concrete columns confined with steel and fibre reinforced polymers." *ACI Struct. J.*, 99(1), 72–80.
- Shinozuka, M., Ghanem, R., Houshmand, B., and Mansouri, B. (2000). "Damage detection in urban areas by SAR imagery." *J. Eng. Mech.*, 126(7), 769–777.
- Shirai, Y. (1987). *Three-dimensional computer vision*, Springer-Verlag, Berlin.
- Shrive, N. G. (2006). "The use of fibre reinforced polymers to improve seismic resistance of masonry." *Constr. Build. Mater.*, 20(4), 269–277.
- Skolnik, M. I. (1990). *Radar Handbook*, McGraw-Hill, New York.
- Soumekh, M. (1999). *Synthetic aperture radar signal processing with MATLAB algorithms*, Wiley, New York.
- Tsang, L., Kong, J. A., and Ding, K.-H. (2000). *Scattering of electromagnetic waves—Theories and applications*, Wiley, New York.
- Yegulalp, A. F. (1999). "Fast backprojection algorithm for synthetic aperture radar." *Proc. IEEE Radar Conf.*, Waltham, MA, 60–65.
- Yu, T.-Y. (2009). *Damage detection of GFRP-concrete systems using electromagnetic waves*, Lambert Academic Publishing, Koln, Germany.
- Yu, T.-Y., and Buyukozturk, O. (2008). "A far-field airborne radar NDT technique for debonding and rebar detection in GFRP-retrofitted concrete structures." *NDT&E Int.*, 41, 10–24.
- Zhao, X.-L., and Zhang, L. (2007). "State-of-the-art review of FRP strengthened steel structures." *Eng. Struct.*, 29(8), 1808–1823.